Materials for Renewable and Sustainable Energy (2025) 14:22
https://doi.org/10.1007/s40243-024-00294-3

ORIGINAL PAPER

Effects of the physisorption properties of human hair-derived activated carbon as a potential electrode for symmetric supercapacitor

Rashed A. M. Adam[1] · Delvina J. Tarimo[1] · Vusani M. Maphiri[1] · Abdulmajid A. Mirghni[1] · Oladepo Fasakin[1] · Ncholu Manyala[1]

Received: 29 September 2024 / Accepted: 29 December 2024 / Published online: 25 February 2025

Abstract

Herein, human hair-derived activated carbon (HH-AC) with remarkable physisorption properties such as high surface area and well-balanced micro- and mesopores, is synthesized by chemical activation method using potassium hydroxide (KOH). The activated carbon is synthesized at different ratio of charred human hair and activator as 1:1, 1:2 and 1:3 for HH AC(11), HH-AC(12) and HH-AC(13), respectively. These activated materials are characterized by a powder X-ray diffraction (XRD), Laser Raman spectroscopy, Scanning electron microscope (SEM), and N_2 adsorption/desorption isotherms. To examine the influence of the micro-mesopore ratio with high surface area on supercapacitor behavior, all samples are tested in a three-electrode using 2.5 moles of potassium nitrate (2.5 M KNO_3) as electrolyte solution. The results show that HH-AC(12) sample which has micro to mesopore-balanced $(50:50)$ exhibited superior electrochemical performance with specific capacitance of $215\,\mathrm{F\,g^{-1}}$ and $125.8\,\mathrm{F\,g^{-1}}$ in the negative and positive potential, respectively at $1\,\mathrm{A\,g^{-1}}$. The sample HH-AC(11), which is dominated by micropores, showed lower rate capability and specific capacitance despite the huge surface area.Whereas the HH-AC(13) sample with mostly mesopores achieved higher rate capability compared to the others. The HH-AC(12) is further examined in a 2-electrode setup to form a symmetric device. The results show a specific energy of $16\,\mathrm{Wh\,kg^{-1}}$ and a specific power of $375\,\mathrm{W\,kg^{-1}}$ at $0.5\,\mathrm{A\,g^{-1}}$. The device demonstrates outstanding capacitance retention of 97% after 10,000 cycles. Thus, ACs with micro to mesopores-balanced are potential candidates for supercapacitor applications.

Keywords Supercapacitor · Activated carbon · Energy storage · Microporous · Mesoporous

Introduction

Electrochemical energy storage (EES) devices include rechargeable batteries, fuel cells, and supercapacitors (SCs) have gained prominence in our modern society due to their use in many applications such as mobile electronic devices, and renewable energy (solar and wind systems) [1, 2]. SCs are popular in EES devices due to their high specific power and long-life span. However, in comparison with batteries and fuel cells, SCs have a relatively low specific energy [3]. The properties of the active electrode include specific surface area (SSA), pore structure, and electrical conductivity are crucial in electrochemical performance of SCs. The type of electrode materials determines the energy storage mechanism, whereby carbonaceous materials, such as activated carbon (AC), single and multi-well carbon nanotubes, graphene (G), and graphene oxide GO), exhibited electric double-layer capacitor (EDLC) behavior [4, 5, 6]. While oxides materials (e.g., manganese dioxide (MnO_2), vanadium oxide (V_2O_5)), and conductive polymers e.g., polyaniline (PANI) show pseudocapacitive behavior [7, 8].

Amongst carbonaceous materials, ACs are widely used as SCs electrode due to their higher SSA, which is the key to the good electrochemical performance of EDLCs. ACs can be produced by physical activation using carbon dioxide (CO_2), steam, or air and chemical activation method with an activating agent such as NaOH, KOH, H_3PO_4, and $ZnCl_2$ [9]. The chemical activation creates more pores and higher mass yield than physical activation [10]. Comparing to other activators, KOH is most effective due to its

✉ Ncholu Manyala
ncholu.manyala@up.ac.za

[1] Department of Physics, University of Pretoria, Pretoria 0002, South Africa

strong basic characteristics and ability to develop micropores and mesopores structure with the high SSA [11, 12, 13, 14]. Therefore, the chemical activation with KOH was selected for the present study.

Common biomass sources for producing activated carbon include coconut shells, wood, and bamboo [15]. In contrast, new biomass sources such as human hair, garlic peels, banana peels, chicken bone, and kapok peels have recently been used to produce ACs for energy storage applications, due to their high SSA, tunable pore structure, and good electrical conductivity [16, 17, 18, 19].

The porous materials are classified by the International Union of Pure and Applied Chemistry (IUPAC) into three families based on pore size diameter: micropores ($< 2\,\mathrm{nm}$), mesopores ($2 - 50\,\mathrm{nm}$), and macropores ($> 50\,\mathrm{nm}$) [20]. The porosity of ACs can be controlled by adjusting the carbonization temperature or the impregnation ratios of the carbon precursor to the activation agent [18, 21]. Previous reports have shown that the type of porosity influences the performance of supercapacitors. For instance, Zhang et al. [22] studied the influence of commercial AC pore structure on the performance of SC and found that AC with an ultramicropore volume ($0.41\,\mathrm{m^3 g^{-1}}$) and a reasonable mesopore volume ($0.15\,\mathrm{m^3 g^{-1}}$) exhibit better electrochemical performance compared to other samples. Also, Liang et al. [18] investigated activated carbon obtained from kapok peels containing both micropores and a mesopores structure. The results showed that ACs has a sheet structure and a high SSA of $\mathrm{S_{BET}} = 1258\,\mathrm{m^2\,g^{-1}}$ consisting of micropore SSA of SSA of S_{mic}=652 m^2 g^{-1} and meso-pore SSA of S_{mes}=606 m^2 g^{-1}, recorded a maximum capacitance of $332.3\,\mathrm{F\,g^{-1}}$ at $1\,\mathrm{A\ g^{-1}}$ in a 3-electrode system. However, there are no explicit studies that have investigated the effects of different micro to mesopores density ratios on activated carbon and correlated them with SC performance. The micropores carbon can provide abundant adsorption sites to absorb ions, but the large number of micropore sites has negative effects on the performance of the supercapacitor because the small pore size partially restricts the diffusion of the electrolyte ions in the electrode, besides, micropore carbon exhibits low-rate capability (low specific capacitance at high specific current) [23]. Consequently, activated carbons with mesopore structures are often used as supercapacitor electrodes because the channels of the mesopores facilitate ion diffusion in the material. However, the high-density ratio of mesopores in the material reduces the SSA [24], which limits the performance of the supercapacitor. Therefore, a synthesized electrode material with balanced micro to mesopores was proposed to utilize both micropores and mesopores for SCs application.

Herein, human hair (HH) was used to synthesize activated carbon, and different concentration of activating agent leading to different micro to mesopore density ratio. Moreover, HH is an abundant source due to the population of human beings and other hairy animals and is considered rich in carbon (approximately 51% of its content is carbon) [25]. The obtained HH-ACs with different micro to mesopore density ratio prepared with different KOH impregnation ratio were used to study their impact on the electrochemical performance of SCs. It is known that combination of micro–mesopores suggests a hierarchical pore structure within the prepared material, which is advantageous for accommodating adsorbate molecules of different sizes. This work reveals various benefits of supercapacitor performance associated with having different micro to mesopore density ratio such as supercapacitor prepared from electroactive material with high mesopore density has a higher rate capability. Amongst the prepared samples, the HH-AC(12) exhibits a balanced micro to mesopore density ratio of ($\mathrm{S_{mic}} = 1696\,\mathrm{m^2\,g^{-1}}$, $\mathrm{S_{mes}} = 1733\,\mathrm{m^2\,g^{-1}}$), which had a higher capacitance performance of $215\,\mathrm{F\,g^{-1}}$ and $125.8\,\mathrm{F\,g^{-1}}$ in negative and positive potential, respectively at $1\,\mathrm{A\,g^{-1}}$, which is higher than other micro to mesopore density ratio combination. This work also illustrates schematic impact of SC performance based on the micro to mesopores density ratio.

Experimental details

Synthesis of activated carbons

Activated carbons were synthesized using chemical activation. The human hair (HH) was collected from a hair salon, cleaned with isopropanol, and dried at 80°C, then carbonized at 300°C for 1.5 h under an argon (Ar) atmosphere (Ar flow rate of 200 cm^3/min and ramping rate of 5°C). The charred HH was crushed and mixed with KOH at a HH : KOH mass ratio of 1:1, 1:2, and 1:3, and drops of deionized water (DW) were added to form a slurry, then the mixture was dried and activated at 800°C for 2 h under an Ar with flow rate of 300 cm^3/min. The activated material was then immersed in 1M HCl for half an hour and washed thoroughly with DW several times until a pH of 7 was reached. Finally, human hair-derived activated carbon (HH-AC) was collected and dried at 80 °C for 12 h. All samples were prepared under the same atmospheric condition. Based on the ratio of HH: KOH which presented as 1:1, 1:2, and 1:3, the samples were given the following notations; HH-AC(11), HH-AC(12), and HH-AC(13), respectively. As shown in Fig. 1, the synthesis is schematically depicted.

The chemical interaction between carbon and KOH can be described by Eq. (1), proposed by Lillo-Ródenas et al. [26].

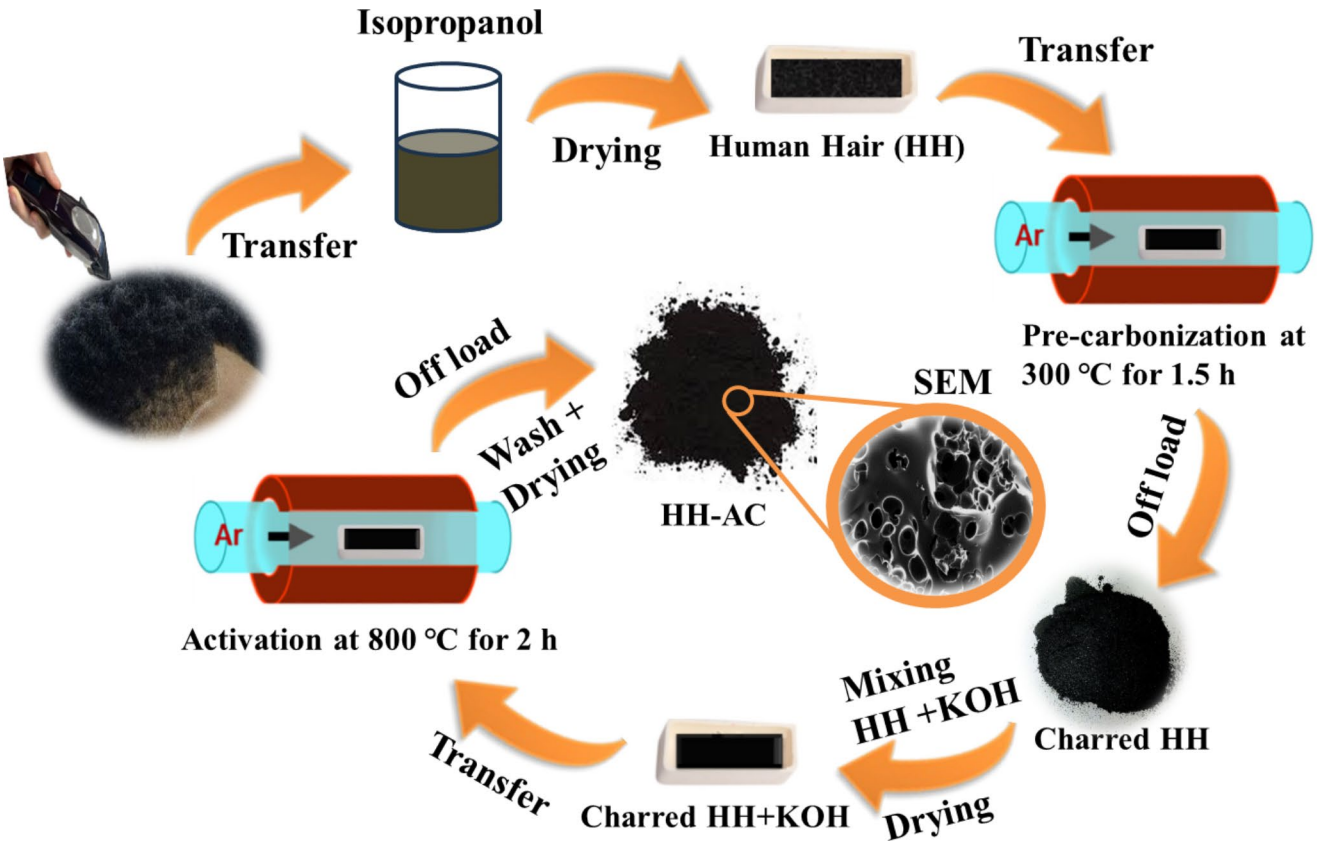

Fig. 1 Schematic representation of HH-ACs synthesis

$$6KOH + 2C \rightarrow 2K + 3H_2 + 2K_2CO_3 \quad (1)$$

Potassium carbonate (K_2CO_3) formed at the temperature around 400°C. The KOH completely consumed when temperature rises to around 600 °C. At temperature above 700 °C, the K_2CO_3 decomposes into the potassium oxide (K_2O) and carbon dioxide (CO_2) (Eq. 2). At temperature around 800 °C, K_2CO_3 or K_2O can react with carbon (C) to produce potassium metal (K) and carbon monoxide (CO) (Eqs. 3 and 4). This reaction produces ACs with a high surface area, as potassium intercalates within the carbon matrix and create pores [27, 28].

$$K_2CO_3 \rightarrow K_2O + CO_2 \quad (2)$$

$$K_2CO_3 + 2C \rightarrow 2K + 3CO \quad (3)$$

$$K_2O + \rightarrow 2K + CO \quad (4)$$

Materials characterization

The materials' structure was identified by XRD (Bruker BV 2D PHASER Best Benchtop) with a Cu Kα radiation. The lattice spacing was estimated using the Bragg's Eq. (1)

$$n\lambda = 2d \sin\theta \quad (5)$$

Where n∼integers (n=1, 2, 3 …), λ∼wavelength of the CuKα radiation ($\lambda = 1.54$ Å), d∼lattice spacing, and θ∼peak centre in rad.

Raman spectra (A WITec alpha 300 RAS+Confocal micro-Raman microscope) using laser wavelength of 532 nm and power of less than 1 mW. The functional groups on the surface of activated carbon were identified using Fourier Transform Infrared Spectrometer (FTIR; JASCO FT/IR-4X). The surface morphology and elemental composition were determined using a field emission scanning electron microscope (FE-SEM; Zeiss Ultra Plus 55, Japan) operated at an accelerating voltage of 2.0 kV. The porosity properties were analyzed using N_2-adsorption/desorption isotherm through NOVA touch (NT 2LX-1, Volts 220 USA) at 77 K, controlled by the Quantachrome TouchWin Software.

Electrochemical evaluations

Electrochemical tests for 3-electrode and 2-electrode configurations were conducted using the Biologic VMP-300 potentiostat (Knoxville TN, USA) operated with EC-Lab V11.50 software. The electrodes were prepared by mixing

80 wt% of HH-ACs, 10 wt% of acetylene carbon black (ACB), and 10 wt% polyvinylidene difluorides (PVDF) then drops of 1-methyl 2-pyrrolidone (NMP) was added to form a slurry. The resulting mixture was coated onto nickel foam (NF, with a thickness of 1.6 mm and areal density of 420 $m^2\ g^{-1}$), in an area of 1.0 1.0 cm^2 for the 3-electrode configuration with a mass loaded of about 2.1 mg for each sample; and a diameter of 1.6 cm for the 2-electrode configuration (with total mass of 3.8 mg) and then dried overnight at 60 ° C. For the 3-electrode test, Ag/AgCl served as a reference electrode (RE), HH-AC sample as an active electrode (working electrode, WE), and carbon glass as a counter electrode (CE). For a 2-electrode configuration, the tests were conducted using a split test cell, with a glass fiber filter serving as a separator between the electrodes. The electrochemical evaluation of the HH-ACs was carried out using cyclic voltammetry (CV), galvanostatic charge-discharge (GCD), and electrochemical impedance spectroscopy (EIS), in 2.5M KNO_3 electrolyte solution. The specific capacitance (C_s) was calculated from the GCD profile using Eq. (6), whereas the specific energy (E_s), specific power (P_s), and maximum power delivered to the load (P_{max}) were calculated using Eqs. (7), (8), and (9), respectively.

$$C_s = \frac{I_s \Delta t}{\Delta V}\ [F\ g^{-1}] \tag{6}$$

$$E_s = \frac{C_s\ (\Delta V)^2}{7.2}\ [Wh\ kg^{-1}] \tag{7}$$

$$P_s = \frac{E_s}{\Delta t}\ x\ 3600\ [W\ kg^{-1}] \tag{8}$$

$$P_{max} = \frac{(\Delta V)^2}{4 m R_i}\ [W\ kg^{-1}] \tag{9}$$

Where, Δt discharge time (s), I_s specific current (A/g), ($I_s = I/m$), I curret (mA), m is the mass loaded (mg), ΔV potential difference (V), and R_i is direct current (DC) internal resistance, ($Note: R_i = \frac{\text{Voltage drop}}{\text{dischagre current}}$) [29].

Results and discussion

Structural, morphological, and elemental analyses

The XRD patterns of HH-ACs are presented in Fig. 2 (a). The samples showed peaks with miller indices of (001), (002), and (100) which correspond to activated carbon material with sp^2 clusters. The (001) and (002) diffraction peaks around 2θ = 11.5-16.5°and 29° indicate the existence of graphite crystallites, while the peak broadness suggests that the prepared material is amorphous [18]. The slight peak of (100) at 2θ=41° indicates that a higher level of graphite interlayer condensation was formed which provides good conductivity. The HH-AC(11) sample shows high peak intensity at 11.5° indicating the presence of high micropore density [17], which decreases with increasing KOH concentration. Based on the (001) diffraction peak, the lattice spacing of HH-AC(11), HH-AC(12) and HH-AC(13) were estimated to be 0.70, 0.62 and 0.53 nm, respectively. While the lattice spacing from the (002) diffraction peak was calculated to be approximately 0.3 nm.

The Raman spectra of the prepared material at the range of 500–3750 cm^{-1} are presented in Fig. 2(b). The de–convoluted Raman spectra within the one phonon region ($800 - 2000\ cm^{-1}$) of the samples are displayed in Fig. 2 (c – e). A total of five bands (D, G, D1, D2, and D3) were observed. The D band refers to the defects and disorders in the carbon matrix, and G band due to the in–plane vibrations of sp^2 hybridized carbon atoms. The D1 peak can be attributed to both $sp^2 - sp^3$ bonds occurring at the edges of sp^2 clusters and ionic impurities. And D2 band is due to the amorphous carbon, while D3 is due to the disorder–induced phonon mode attributed to the pentagonal and octagonal rings crystal defects caused by vacancy [30, 31]. D band to G band ratio (I_D/I_G) of an integrated area of HH-AC(11), AC(12) and HH-AC(13) was calculated to be 4.7, 4.05, and 3.93, respectively. It appears that the concentration of the activator inversely proportional to the degree of defect and the dominance of (001) diffraction peak. The Tuinstra – Koenig model [32] relates I_D/I_G to average crystallite size L_a (average sp^2 cluster) using Knight Formula (10)

$$L_a = \frac{C(\lambda)}{I_D/I_G}\ [nm] \tag{10}$$

where $C(\lambda)$ is the wavelength–dependent pre – factor ($C(\lambda) \approx C_o + \lambda C_1$), for 400 < λ < 700 nm the C_1 and $C_o$were estimated to be 0.033 nm and −12.6 nm, respectively. The wavelength used in this study is $\lambda = 532$ nm, therefore $C(\lambda) = 4.96$ nm. L_a for HH-AC(11) sample, HH-AC(12), and HH-AC(13) was calculated to be 1.04, 1.22, and 1.26 nm, respectively. This suggests that size of the carbon crystal depends strongly on the concentration of the activating agents.

The FTIR spectra of HH-ACs samples are shown on Fig. 2(f), it is seen that all samples exhibited similar surface functional groups. The broad peak at 3000–3600 cm^{-1} referring to the O-H stretching vibration mode of absorbed water molecules. The peaks at 1542 cm^{-1} and 1065 cm^{-1} correspond to the C=C bonds of aromatic compounds and

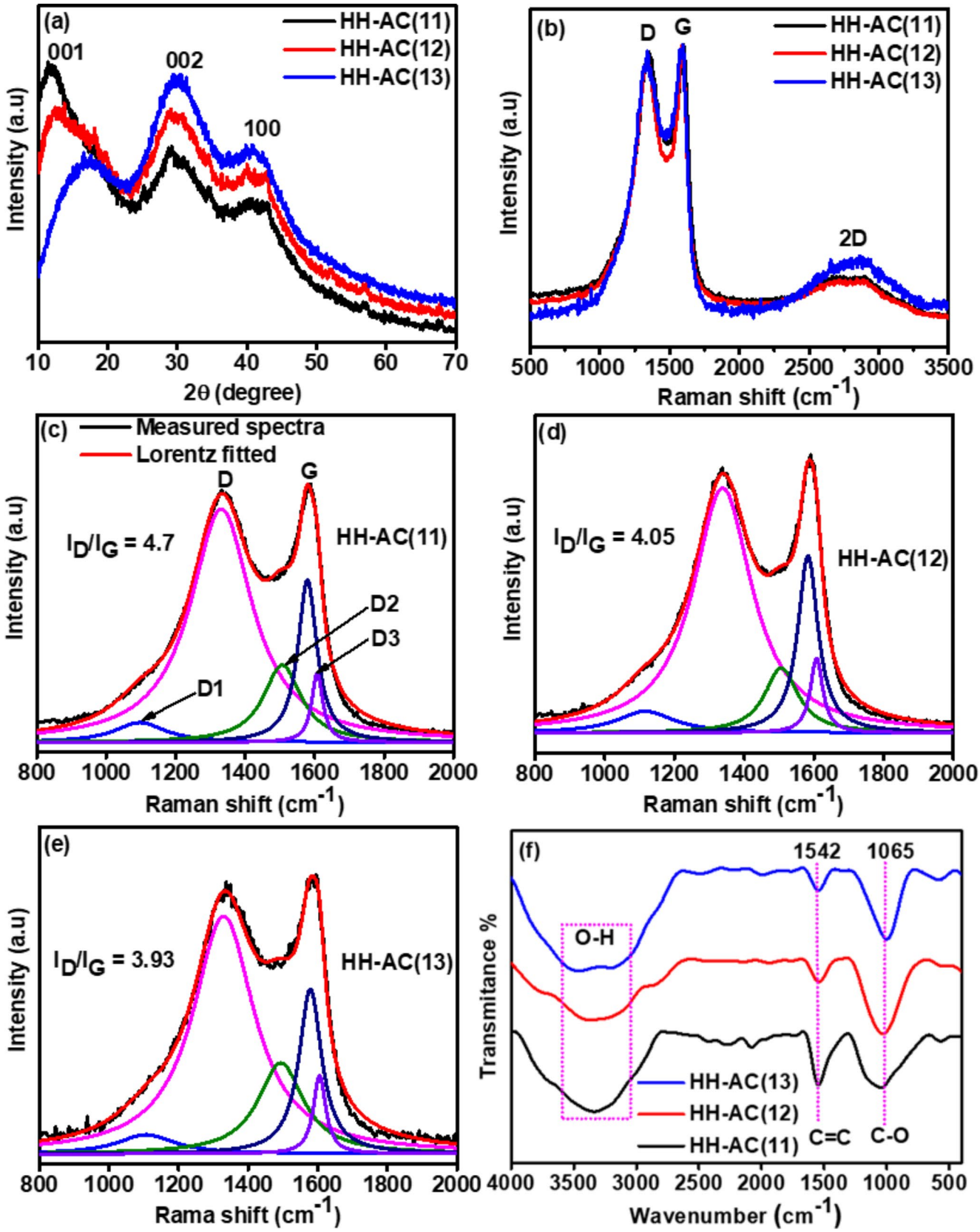

Fig. 2 (**a**) XRD pattern of HH-ACs, (**b**) Raman full spectra, (**c**-**e**) the de–convoluted Raman spectra of HH-AC (11), HH-AC (12), and HH-AC (13), respectively. (**f**) FTIR spectra

C-O stretching vibration of carboxylic acid, respectively [33, 34].

The surface morphologies of the materials were examined by SEM, the images are seen in Fig. 3. The samples showed a spongy-like with an irregular surface. The HH-AC(11) in Fig. 3 (a, b) has numerous cavities of small size. These features are expected to provide a higher surface area. In contrast, HH-AC(12) in Fig. 3 (c, d) has a moderate cavity size and a modest number of cavities compared to others. Whereas the HH-AC(13) sample in Fig. 3 (e, f) has a smaller number of cavities and most of its cavity sizes are bigger than the others, this may be attributed to the high concentration of KOH, which is more aggressive and increases pores size.

The energy dispersive x-ray (EDX) was carried out to determine the elemental composition of the raw material (human hair) and HH-ACs samples (Fig. S1). The results show that the Human hair contains 62% carbon (C), 16.5%

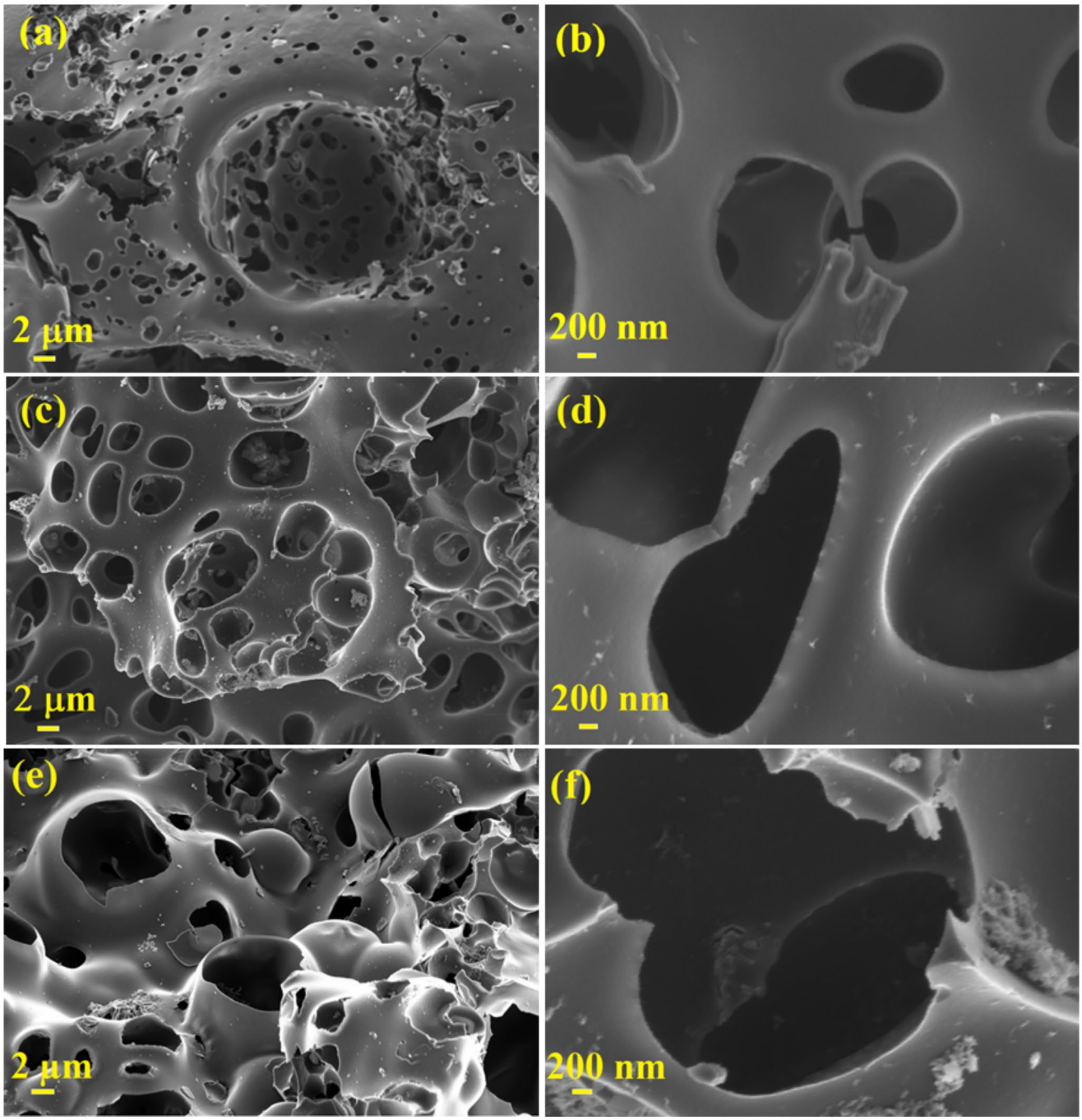

Fig. 3 SEM images at low and high magnification: (**a**, **b**) For HH-AC(11), (**c**, **d**) for HH-AC(12), and (**e**, **f**) for HH-AC(13), respectively

nitrogen (N), 11% oxygen (O), 9% sulphur (S), and 1.5% other elements (Ca, Mg, and Na). In contrast, HH-ACs samples contain between 88 and 90% carbon, 10–11% oxygen, and a tiny amount of S and silicon (Si). S comes from human hair, whereas Si is because of ash contained in the samples during the activation [35].

Textural properties

The N_2-adsorption/desorption isotherms are illustrated in Fig. 4 (a). All samples have the hysteresis loops of type IV isotherms. The HH-AC(11) sample shows high adsorption at low relative pressures, suggesting numerous micropores. At a relative pressure (P/P_0) in the range (0.3-1.0), a tiny hysteresis loop is observed, indicating a certain amount of mesopores. As the impregnation ratio of prepared materials increases from 1:1 to 1:3, the hysteresis loops gradually widen, as can be seen more clearly in the inset of Fig. 4 (a), indicating that activated carbon is populated with mesopores [9]. Figure 4 (b) shows the percentage contribution of micropores and mesopores to the Brunauer-Emmett-Teller (BET) surface area of HH-AC(11), HH-AC(12) and HH-AC(13). The figure shows that HH-AC(11) has 80% micropores and 20% mesopores, and HH-AC(12) has 49.5% micropores and 50.5% mesopores which means that this particular sample has the balance between micro and mesopores. The HH-AC(13) has mostly mesopores with 23.3% micropores and 76.7% mesopores. These percentages indicate a very important result, which is that as the ratio of HH material to KOH changes from 1:1 to 1:3, the percentage of mesopores increases, and this may have a significant impact on the electrochemical results. The BET plot of HH-ACs sample was shown in (Fig. S2) with correlation coefficient of 0.999 which indicates a perfect linear relationship between relative pressure (P/P_o) and $1/[w((P/P_o)-1)]$, where w is amount of N_2 gas adsorbed at a given (P/P_o). Figure 4(c) shows the pore size distribution (PSD) of HH-ACs samples calculated using non-local density functional theory (NLDFT). The HH-AC(11) sample recorded strong peaks in the range of (1–2 nm), suggesting a significant number of micropores in this material, while HH-AC(12) has moderate peaks in the micropores (1–2 nm) and mesopores (2–4 nm) regions, indicating a balanced distribution of micro- and mesopores. The HH-AC(13) sample shows a broad peak at around 3.5 nm with a higher differential pore volume than others, indicating that most of this material is composed of mesopores. In Fig. 4(d), quenched solid density functional theory (QSDFT) is used to calculate the PSDs of HH-AC samples. It is shown that in the micropores region, the HH-AC(11) sample has the high differential pore volume followed by HH-AC(12) and then HH-AC(13) which follow the same trend as in the NLDFT. Comparing QSDFT with NLDFT, it is observed that the PSD curve of QSDFT has a confidence limit of around 0.61 nm, whereas the PSD curve of NLDFT has a confidence limit of around 1.5 nm, which indicates an artificial gap in NLDFT at small pore sizes; also, the sharp minimum peak at around 2 nm or less, appeared in the PSD curve calculated by NLDFT, because of the mono-layer transition on the smooth graphite surface which is vanished in the QSDFT pore size distribution curve because QSDFT takes into account the pore wall roughness and defect of the surface, which is not considered in NLDFT [36]. A comparison of SSA calculated by NLDFT and QSDFT is shown in Fig. 4(e). It is showing that the surface area calculated by QSDFT is higher in all cases of the samples than that calculated by NLDFT, which reflects the result of the PSD curve, showing that QSDFT has ability to cover a pore with a pore diameter of 0.61 nm.

Table 1 shows important porosity parameters of HH-ACs samples. It is seen that as the impregnation ratio increases, the SSA decreases while the total pore volume increases. This may be due to the dominance of mesopores and a decrease in micropores. In addition, the average pore diameter is also increasing, further suggesting that the porosity is changing from micropores to mesopores. According to these findings, the pore size of activated carbon increases with increasing KOH usage in the chemical activation process. This is because of several mechanisms that enhance porosity. The potassium compounds, especially metallic potassium (K), intercalate into the carbon matrix, expanding and disrupting the carbon structure. A network of pores is formed in the carbon matrix during this etching process, which becomes more pronounced with increasing KOH concentration, resulting in larger pore sizes. The use of KOH activation normally produces micropores. However, as the KOH concentration increases, the etching becomes more aggressive, widening existing micropores and forming mesopores (2–50 nm) [37].

Electrochemical performance

Three electrodes system

Figure 5 shows the electrochemical performance of HH-ACs samples in 3-electrode systems. The material operates in a positive potential range of 0.0 to 0.7 V and a negative potential range of -0.8 to 0.0 V at $20\ \mathrm{mV\ s^{-1}}$ as shown in Fig. 5 (a-d). The CV curves of the positive and negative potentials shown in Fig. 5 (a, b) exhibit a quasi-rectangular shape, indicating the EDLC behavior of the synthesized material. From the CV curves in Fig. 5(a, b), it can be seen that the sample HH-AC(12) displayed a higher current response compared to HH-AC(11) and HH-AC(13). Figure 5 (c, d) compares GCD curves at $1\ \mathrm{A\ g^{-1}}$. The GCD

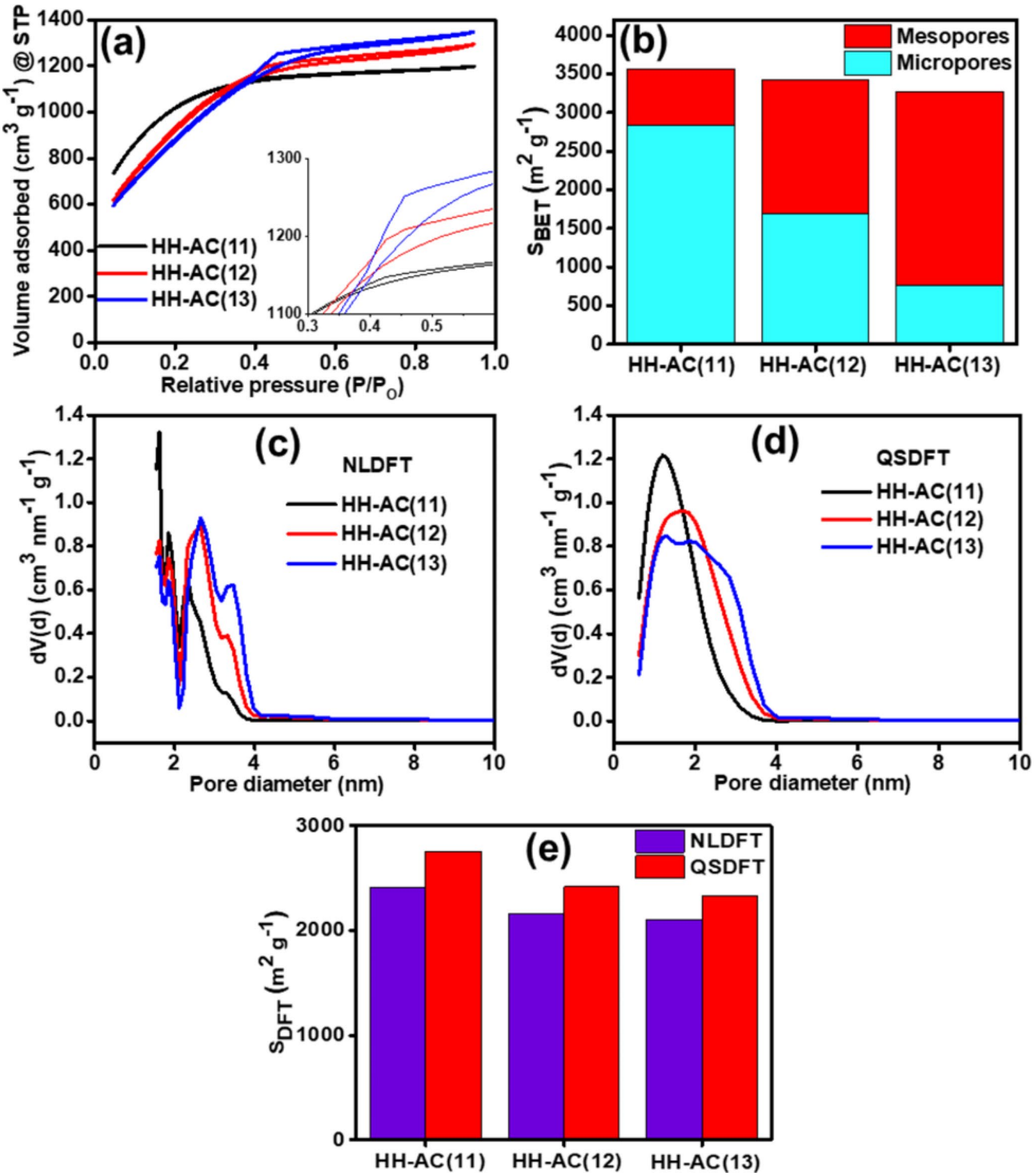

Fig. 4 (**a**) N_2-adsorption/desorption isotherms, (**b**) the percentage contribution of micropores and mesopores to the BET surface area, (**c**, **d**) PSD using NLDFT and QSDFT (**e**) a comparison of SSA calculated using NLDFT and QSDFT

curves showed the symmetric triangular linear characteristics, which were consistent with the CV curves in Fig. 5 (a). From GCD in Fig. 5 (c, d), sample HH-AC(12) has a longer discharge time, unlike samples HH-AC(11) and HH-AC(13) which is in good agreement with the CV curves confirming the sample's higher storage capability. Figure 5 (e, f) shows the values of capacitance at different currents ranging from 1 to 10 A g^{-1} in the positive and negative potential,

Table 1 Porosity parameters of HH-ACs samples

Parameter	HH-AC(11)	HH-AC(12)	HH-AC(13)
S_{BET} $\left(m^2\ g^{-1}\right)$	3564	3429	3272
S_{mic} $\left(m^2\ g^{-1}\right)$	2834	1696	762
S_{mes} $\left(m^2\ g^{-1}\right)$	730	1733	2510
V_t $\left(cm^3\ g^{-1}\right)$	1.86	2.0	2.1
V_{mic} $\left(cm^3\ g^{-1}\right)$	1.34	0.80	0.34
V_{mes} $\left(cm^3\ g^{-1}\right)$	0.52	1.20	1.76
D_{50} (nm)	2.10	2.34	2.55
S_{NLDFT} $\left(m^2\ g^{-1}\right)$	2412	2165	2106
S_{QSDFT} $\left(m^2\ g^{-1}\right)$	2756	2419	2329

S_{BET}~ surface area calculated from Brunauer, Emmett, and Teller theory; S_{mic}~ micropores surface area; S_{mes}~ mesopores surface area; V_t, V_{mic}, and V_{mes} are total, micro, and meso-pore volume, respectively, and D_{50}~ average pore diameter. S_{NLDFT}, and S_{QSDFT} are specific surface area calculated using NLDFT and QSDFT

respectively. The results show that the HH-AC(12) sample has a higher specific capacitance which corresponds to the CV and GCD curves. It is observed that despite the high SSA, HH-AC(11) delivers lower specific capacitance compared to the other samples. This may be due to the small number of mesopores in this sample (80% micropores and 20% mesopores, as shown in Fig. 4 (d)) which restricts the movement of ions [38]. A considerable increase in specific capacitance was observed in the HH-AC(12) sample, which has approximately the same percentage of mesopores (50.5%) and micropores (49.5%), which facilitate ion diffusion and charge accommodation, respectively [39]. As the mesopores further increase to 76.7% and the micropores decrease to 23.3% (sample: HH-AC(13)), the capacitance was found to decrease due to the large number of mesopore sites, resulting in a lower specific surface area compared to HH-AC(11), and HH-AC(12) samples. In terms of rate capability, the HH-AC(13) sample shows a higher rate capability of 91% and 86.6% in positive and negative potentials, respectively at 10 A g^{-1}, HH-AC(12) demonstrated almost the balanced rate capabilities of 87.2% and 82.6% for positive and negative potentials, respectively due to balanced micro to meso pores ratio, while HH-AC(11) sample exhibited a lower rate capability of 74.2% and 78.7% in positive and negative potentials, respectively. The low rate capability of HH-AC(11) sample can be attributed to its high micropore content, which limits the ability of ions to penetrate into the very small pores. Moreover, the capacitance difference in the positive and negative potential may be attributed to the ion's size, where the ion size of K^+ is 1.33 Å and for NO_3^- is 2.64 Å [40]. The CV curves at various scan rates ($5-300\ mV\ s^{-1}$) for all samples were provided in Fig. S3. (Supporting information). These CVs were used to estimate the contribution of non–diffusion capacitance ($C_{non-diffu}$) and diffusion capacitance (C_{diffu}), using Trasatti's analysis Eqs. (S1) – (S3) and displayed in Fig. S4. All the prepared samples have a similar non–diffusion and diffusion capacitance contribution, which accounts for about 87% and 13% of the total capacitance (C_T), respectively, which shows that the capacitance behavior within this work is affected by micro – mesopore density ratio. The volumetric capacitances in $F\ cm^{-3}$ were also calculated for all samples at positive and negative potential, yet the sample with micro/mesopores balance has higher volumetric capacitance followed by HH-AC(13) and HH-AC(11) samples (Table S1).

Nyquist plot displayed in Fig. 5 (g) was done in a frequency range of 100 kHz–10 mHz with voltage amplitude of 10 mV. The inset to the figure shows the magnified high–frequency region. An intercept on the X-axis in the high-frequency region refers to equivalent series resistance (ESR), the figure shows the ESR values of HH-AC(11), HH-AC(12), and HH-AC(13) as 1.2, 0.89, and 0.64 **Ω**, respectively. The low ESR of the HH-AC(13) is due to the mesopore structure of the sample, which facilitates the movement of ions. The diameter of the arc at intermediate frequency zone is associated with the charge transfer resistance (R_{ct}) across the electrode – electrolyte interface. In the lower frequency region, it can be seen that HH-AC(12) has a shorter diffusion length and also closer to the Y-axis, suggesting superior capacitive behavior [41]. Figure 5 (h) represents capacitance retention and Columbic efficiency vs. cycle number performed for 5000 cycles at $5\ A\ g^{-1}$. All samples have Coulombic efficiency of approximately 100% with no significant degradation noticed. However, slightly different values of capacitance retention of the samples were observed with HH-AC(11), HH-AC(12) and HH-AC(13) as 96%, 91% and 89% of the initial capacitances, respectively. These stability tests prove that the prepared materials are electrochemically stable.

Electrochemical correlation

A schematic summary of the obtained results from the material preparation to the electrochemical performance is shown in Fig. 6. It was mentioned above that the locally collected human hair shown on Fig. 6 (a1) was charred (Fig. 6 (a2)) through pre–carbonization process, and then activated with KOH at different HH: KOH mass ratios of 1:1, 1:2, and 1:3. The XRD shows that as the KOH activating agent increases, the micropore density and its size also decrease.

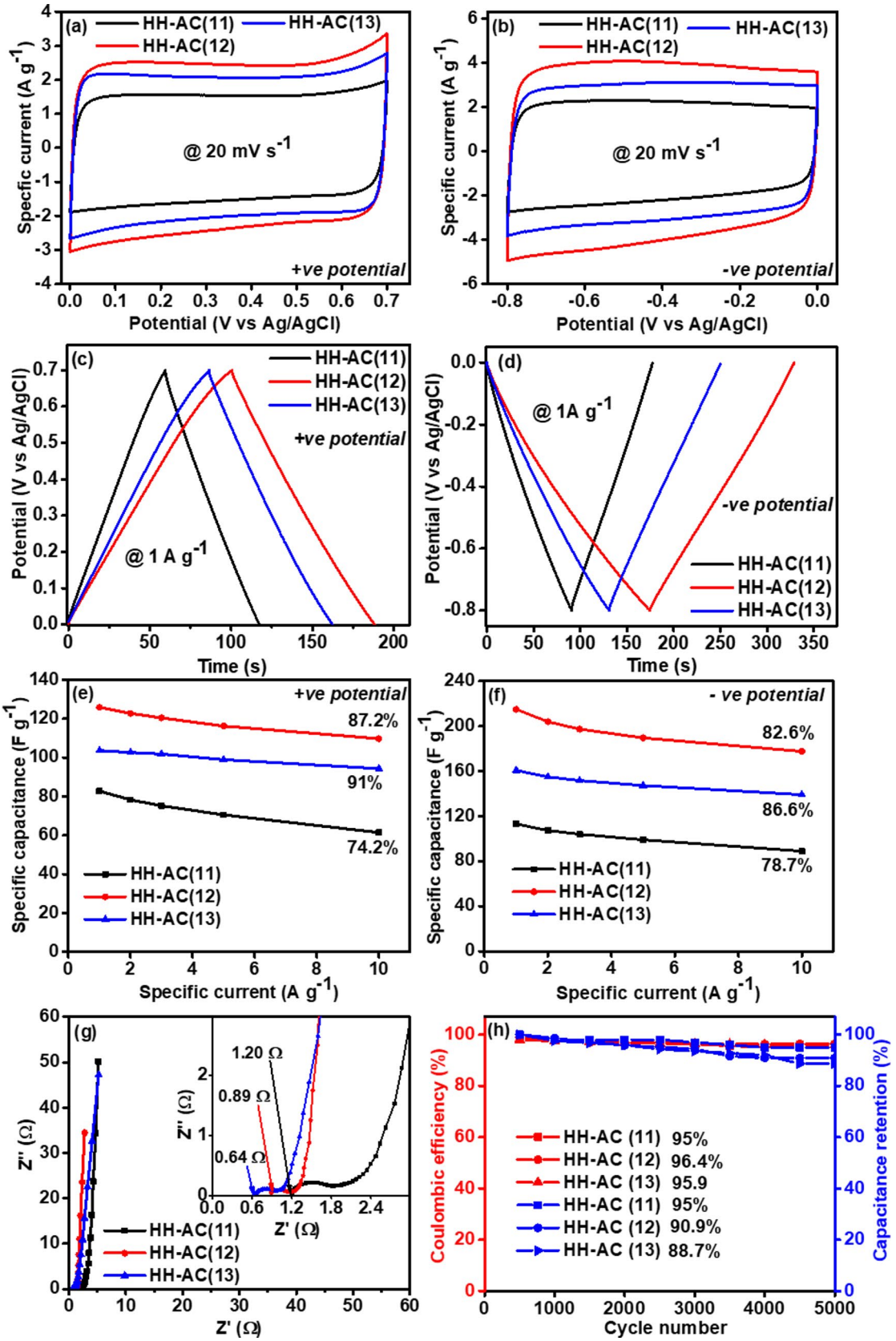

Fig. 5 Electrochemical performance of HH-ACs in 3-electrode system; (**a**, **b**) CV curves, (**c**, **d**) GCD profile, (**e**, **f**) specific capacitance vs. specific current at the positive and negative potential, respectively, (**g**) Nyquist plot, and (**h**) cycling stability

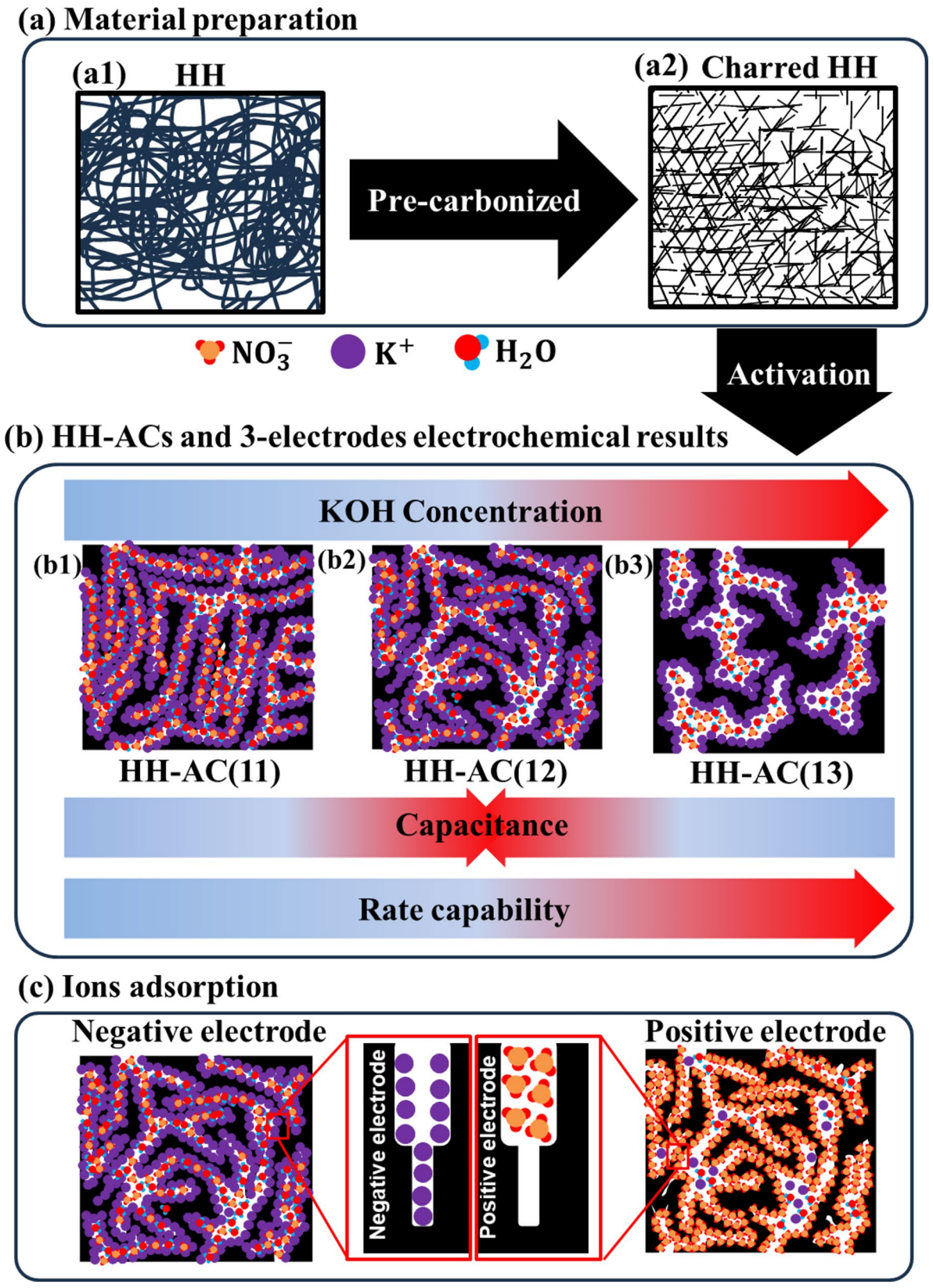

Fig. 6 Schematic summary from material preparation to electrochemical results

The SEM results showed that the observable pores sizes also increase with increasing KOH concentration, but pore density decreases. The pores (cavities) observed in SEM were quantified using (N_2) gas adsorption. The micropore density decreased with increasing KOH, while the mesopore density increased. This behaviour can be attributed to the fact that higher KOH concentrations are more aggressive and resulting in wide pore structures. This difference in micro–mesopore density ratio impacts the electrochemical behavior of the AC. It is well known that micropores are responsible for ion adsorption, while mesopores act as an ion passage connecting macropore reservoirs. Theoretically, HH-AC(11) (Fig. 6 (b1)) with a the highest surface area and micropore density should show the highest capacitance, which is different from the observed results, which can be attributed to bigger electrolyte ions not utilizing the small micropores and also ion mobility. The HH: AC(12) (Fig. 6 (b2)) with a micro–mesopore density ratio of almost 50:50% showed the highest specific capacitance due to the appropriate micropore size and sufficient mesopores allowing enough ion mobility, while HH: AC(13) have a lower capacitance due to the small micropore density. This capacitance behavior can be seen in Fig. 5 (a) – (f). The rate capability retention at 10 A g^{-1} for both potential windows shown in Fig. 5 (e) and (f), which shows that the rate capability retention increases with increasing mesopores due to easy ions mobility, as shown in Fig. 6 (b1) – (b3). This is also supported by ESR reduction attributed to easy ion mobility due to increased mesopore density. Moreover, Fig. 6 (c) illustrates the difference in the obtained capacitance in the positive and negative potential. In negative potential, the smaller K^+ ions are adsorbed easily on the micropores, while bigger NO_3^- ions have difficulty fitting into the pores that K^+ would easily do. Thus, this leads to a drop-in capacitance in the positive.

Two electrode system

The HH-AC(12) sample showed superior electrochemical performance compared to HH-AC(11) and HH-AC(13) in both negative and positive potential windows. This material was further subjected to a two–electrode test for a symmetric device (HH-AC(12)//HH-AC(12)) as shown in Fig. 7. Since the material performs differently in positive and negative potential, a charge–balance was carried out to adjust the amount of mass to be loaded in both electrodes in the device using Eq. (11).

$$\frac{m_+}{m_-} = \frac{C_{S-} \times \Delta V_-}{C_{S+} \times \Delta V_+} \tag{11}$$

Where m_+ and m_- are the positive and negative mass of active electrodes, C_{S+}, C_{S-}, V_+, and V_- are specific capacitances and potential difference for the positive and negative electrodes, respectively. According to Eq. (11), the m_+ and m_- were estimated to be 2.3 and 1.5 mg, therefore the total mass is 3.8 mg.

The fabricated symmetric device was tested under voltage window of 1.5 V. Figure 7 (a) shows the CV curves of the HH-AC(12)//HH-AC(12) symmetric device at different scan rates (5 to 200 mV s^{-1}). The device performed significantly at its expected potential of 1.5 V, translating the accumulation of 0.0 to 0.7 V vs. Ag/AgCl in a positive potential and − 0.8 to 0.0 V vs. Ag/AgCl in a negative potential. The CV curves show a semi–rectangular shape even at higher scan rates of 200 mV s^{-1} and maintain the same shape without significant change, indicating excellent rate capability. Figure 7 (b) illustrates the GCD curves of the symmetric HH-AC(12)//HH-AC(12) device with triangular shapes at various currents ranging from 0.5 to 10 A g^{-1} and shows an accurate consistency with the CV in Fig. 7 (a). At a specific current of 0.5 A g^{-1}, a small IR drop of 0.0038 V was observed, confirming the ideal capacitive behaviour and low ESR of the device. Figure 7 (c) demonstrates specific capacitance of the symmetric device HH-AC(12)// HH-AC(12) at different specific currents. The device recorded specific capacitance values of 51.26, 49.47, 48.16, 46.94, 44.87, and 40.67 F g^{-1} at specific currents of 0.5, 1, 2, 3, 5 and 10 A g^{-1}. Remarkably, the device retained 79% of its specific capacitance between 0.5 A g^{-1} (51.26 F g^{-1}) and 10 A g^{-1} (40.67 F g^{-1}) indicating an excellent rate capability for HH-AC(12)//HH-AC(12) symmetric device. Long term cycle stability of the symmetric device HH-AC(12)// HH-AC(12) was achieved. A capacitance of 97% was retained after 10,000 cycles at 5 A g^{-1}, while the columbic efficiency was remained at ~100% indicating a good electrochemical stability of the HH-AC(12)//HH-AC(12) symmetric device. Figure 7 (e) displayed a Ragone plot of different supercapacitor devices using ACs as electrode material in an aqueous electrolyte. The data for the Ragone plot were collected from Refs [42, 43, 44, 45, 19], and [46]. As illustrated in the Ragone plot, the symmetric device in the present work showed E_S of 16 Wh kg^{-1} and P_s of 375 W kg^{-1} at 0.5 Ag^{-1}. Table 2 shows the comparison of the specific capacitance of the SC devices using ACs from different sources as electrodes material in an aqueous electrolyte. The present work exhibited a high SSA, high specific capacitance, and good voltage window compared to ACs derived from other sources (precursor).

Figure 8 (a) represents a Nyquist plot of experimental and fitted data performed in a frequency range of 100 kHz–10 mHz and voltage amplitude of 10 mV. The insets in Fig. 8 (a) display the magnified high–frequency zone and the equivalent circuit used for the fitting. The circuit diagram contains the following elements: ESR, capacitor (C),

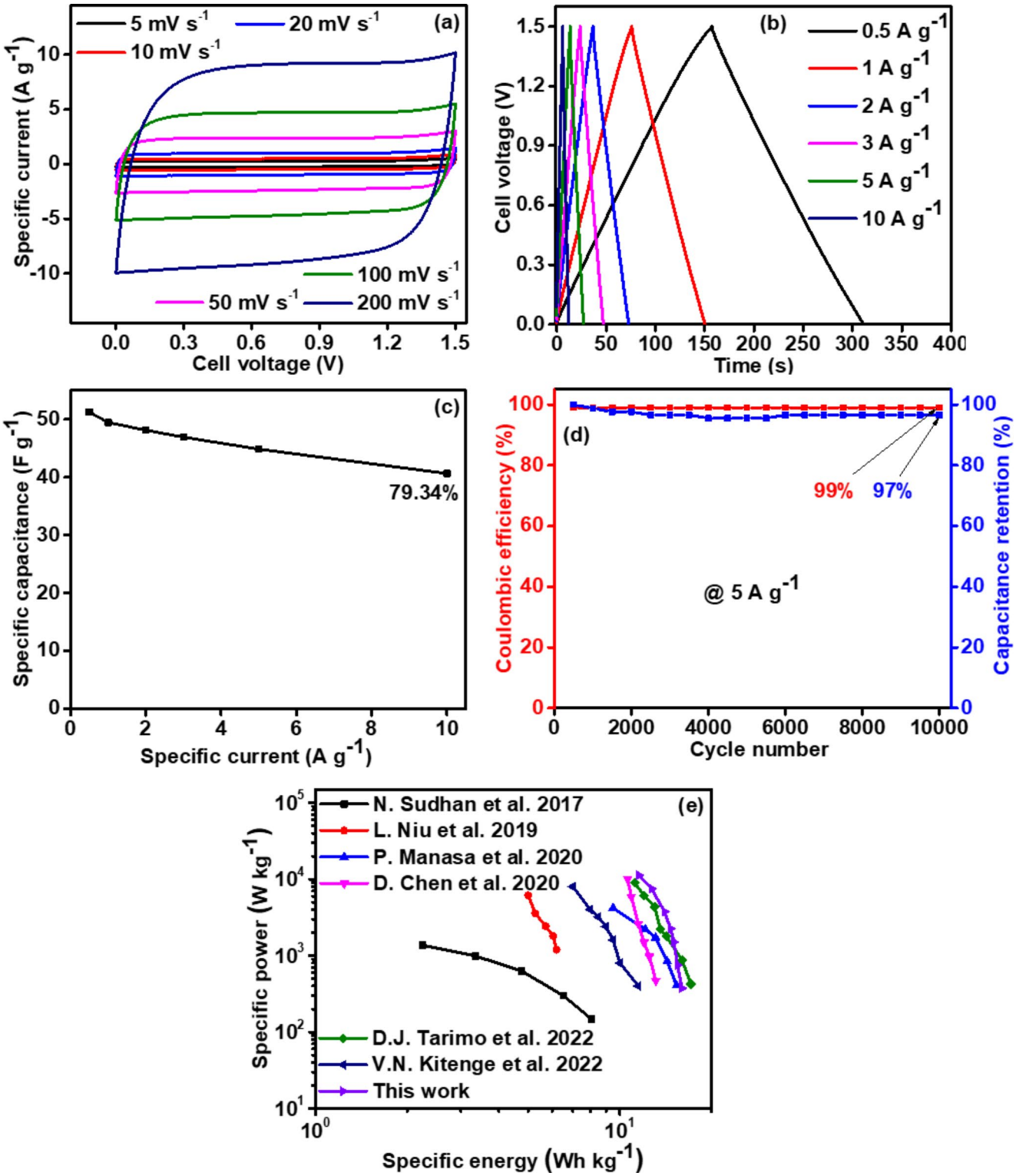

Fig. 7 Electrochemical performance of HH-AC(12)//HH-AC(12) symmetric device: (**a**) CV curves, (**b**) GCD profile, (**c**) specific capacitance vs. current, (**d**) cyclic stability and (**e**) Ragone plot

Table 2 A comparison of the capacitance of the symmetric SCs devices using AC from different sources as electrodes in aqueous electrolyte

Precursor	AA	SSA ($m\ g^{-1}$)	Electrolyte	VW (V)	SEC ($F\ g^{-1}$)	Ref.
Rice straw	KOH	1007	1 M H_2SO_4	1.2	156 @ 0.5 A g^{-1}	[42]
Waste Pork bones	KOH	1260	6 M KOH	1.2	133 @ 1 A g^{-1}	[43]
Chicken bone	KOH	2236	1 M $NaNO_3$	1.7	170.41 @ 0.5 A g^{-1}	[19]
Mangosteen shell	K_2CO_3	2803	2.5 M KNO_3	1.6	129.36 @ 0.5 A g^{-1}	[46]
Carchorus Olitorius	KOH	1903	1 M Na_2SO_4	1.6	173.7 @ 0.5 A g^{-1}	[44]
Banana peels	KOH	1362	1 M $NaNO_3$	1.8	165 @ 0.5 A g^{-1}	[47]
Human hair	KOH	3429	2.5 M KNO_3	1.5	205.2 @ 0.5 A g^{-1}	This work

AA ~ Activating agent, **SSA** ~ Specific surface area, **VW** ~ Voltage window, **SEC** ~ Single electrode capacitance. [Note that SEC =4×capacitance of the cell (device)]

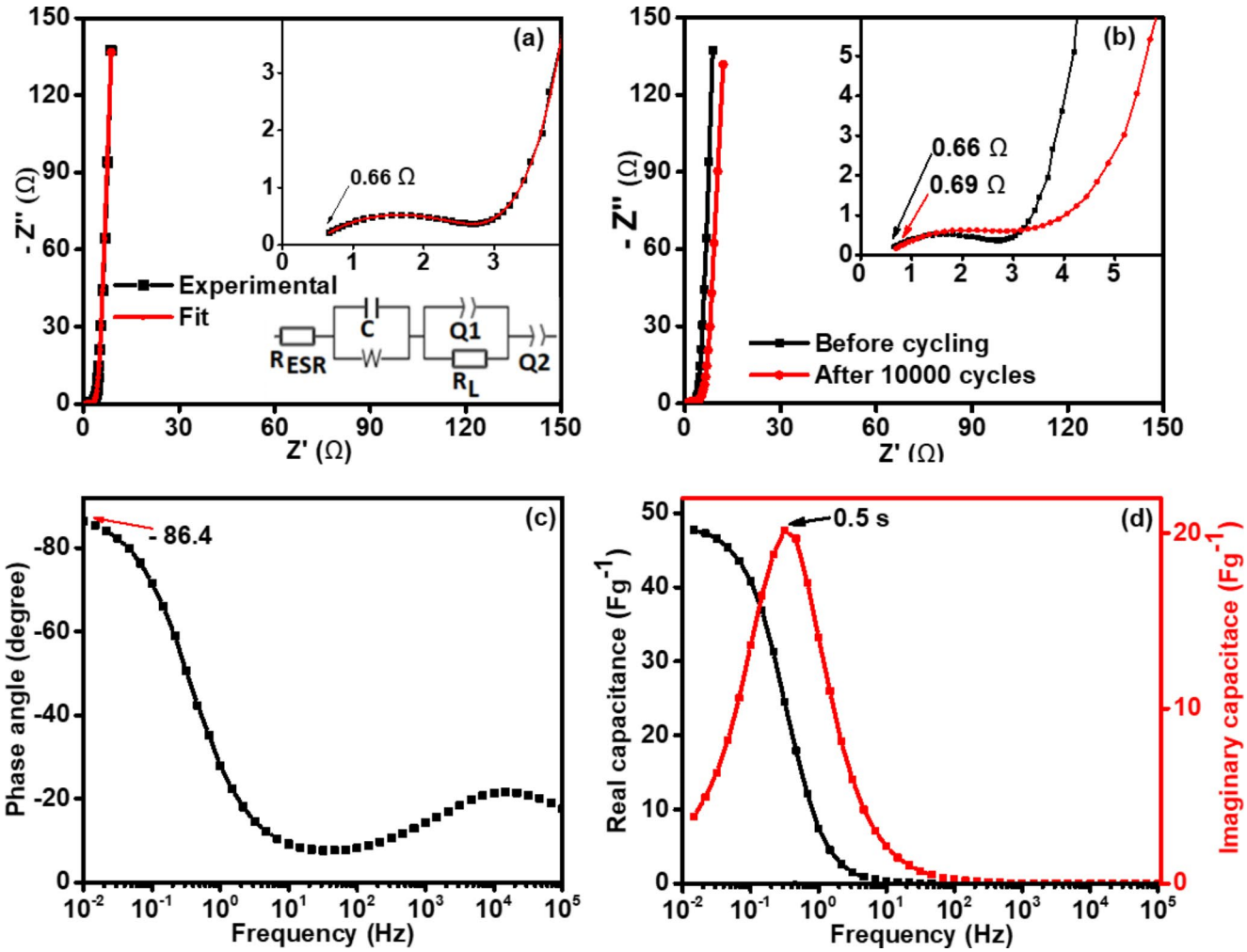

Fig. 8 (**a**) Nyquist plot (the inset is an equivalent fitting circuit), (**b**) Nyquist plot before and after cycling, (**c**) Bode plot, and (**d**) Real and imaginary capacitance versus frequency of HH-AC(12)//HH-AC(12) symmetric device

Warburg impedance (W), leakage resistance (R_L), and constant phase element (Q1 and Q2). The experimental and fitted ESR values were estimated to be 0.66 Ω and 0.67 Ω, respectively, giving almost the same values, indicating proper fitting. The lower ESR value is confirmed by the very small IR drops seen in the GCD profiles. The R_{ct} at the electrode-electrolyte interface is 2.15 Ω. This small value makes the ions move easily.

The DC internal resistance (R_i) was calculated to be 2.11 Ohm, based on the slope of the voltage drop vs. applied current curve (Fig. S5). Therefore, the maximum power delivered to the load was calculated to be $71\ kW\ kg^{-1}$ using Eq. (9). In addition, Fig. 8 (b) displays the Nyquist plot

before and after 10,000 cycles. The figure shows that there is no big difference between the ESR values before and after cycling, and the deviation of the Nyquist plot on the y-axis is very small, indicating higher durability of the device. The Bode plot in Fig. 8 (c) shows that at the lower frequency, the corresponding phase angle is $-86.4\,^{\circ}$, which is very close to the ideal phase angle of $-90\,^{\circ}$ indicating a higher capacitance capability.

Figure 8 (d) displays the frequency versus real and imaginary capacitance. The real capacitance (C') values and imaginary capacitance (C'') values were calculated using the following Eq.

$$|Z(\omega)|^2 = (Z')^2 + (Z'')^2 \tag{12}$$

$$C' = Z''/\omega|Z(\omega)|^2 \tag{13}$$

$$C'' = Z'/\omega|Z(\omega)|^2 \tag{14}$$

Z is the resultant impedance, Z', and Z'' are the real and imaginary impedances, respectively, ($= 2f$) is the angular frequency. The relaxation time (τ) of 0.5 s was calculated from the relation of $2\pi f_o \tau = 1$. Where f_o is the frequency corresponding to the maximum imaginary capacitance. This relaxation time is relatively short compared with some carbon-based supercapacitor electrodes that already reported in the literature [48, 49, 50] which indicates a fast ion diffusion into the active electrode material [22].

Conclusion

Human hair-derived activated carbon with high SSA were successfully synthesized using chemical activation. The pore structure was controlled by varying the impregnation ratio between human hair (HH) and potassium hydroxide (KOH). As the KOH concentration increases, the proportion of mesopores increases and the proportion of micropores decreases. The BET specific surface areas of HH-AC(11), HH-AC(12), and HH-AC(13) were calculated to be 3564, 3429, and 3272 $m^2\,g^{-1}$, respectively. The electrochemical results show that the HH-AC(12) sample with the micro/mesopores balance had a higher specific capacitance than other samples at positive and negative potential in the three-electrode configurations. The symmetric supercapacitor HH-AC(12)//HH-AC(12) recorded a specific energy of $16\,Wh\,kg^{-1}$ and a corresponding power of $375\,W\,kg^{-1}$. Based on the obtained results, activated carbon with balanced porosity is a potential candidate for use in supercapacitors application. This study demonstrates that the excellent electrochemical performance of SCs is not solely determined by the SSA of active material. The findings indicate that the PSD and surface morphology of the material are also significant factors that contribute to the overall electrochemical performance of SCs.

Supplementary Information The online version contains supplementary material available at https://doi.org/10.1007/s40243-024-00294-3.

Acknowledgements The authors thank the University of Pretoria for financial and infrastructural support. The lead author would like to thank his home institution, the University of Alfashir, for financial support.

Declarations

Competing interests The authors state that there are no known competing financial interests or interpersonal connections that could have influenced the work reported in this paper.

References

1. Dawoud, H.D., Al Tahtamouni, T., Bensalah, N.: Sputtered manganese oxide thin film on carbon nanotubes sheet as a flexible and binder-free electrode for supercapacitors. Int. J. Energy Res. **43**, 1245–1254 (2019). https://doi.org/10.1002/er.4364
2. Manjakkal, L., Jain, A., Nandy, S., Goswami, S., Tiago Carvalho, J., Pereira, L., See, C.H., Pillai, S.C., Hogg, R.A.: Sustainable electrochemical energy storage devices using natural bast fibres. Chem. Eng. J. **465** (2023). https://doi.org/10.1016/j.cej.2023.142845
3. Gao, L., Chen, Z., Zhao, H., Zou, Y., Yu, C., Zhong, W.: Controllable preparation of nitrogen-doped hierarchical and honeycomb-like porous carbon/graphene based on composites of graphene oxide and polyaniline nanorod arrays for high performance supercapacitors. J. Energy Storage. **36**, 102314 (2021). https://doi.org/10.1016/j.est.2021.102314
4. Kwak, C.H., Kim, D., Bai, B.C.: Correlation of EDLC Capacitance with Physical properties of Polyethylene Terephthalate added Pitch-based activated Carbon. Molecules. **27**, 1–13 (2022). https://doi.org/10.3390/molecules27041454
5. Zhou, Y., Jin, P., Zhou, Y., Zhu, Y.: High-performance symmetric supercapacitors based on carbon nanotube/graphite nanofiber nanocomposites. Sci. Rep. **8**, 1–8 (2018). https://doi.org/10.1038/s41598-018-27460-8
6. Liu, C., Yu, Z., Neff, D., Zhamu, A., Jang, B.Z.: Graphene-based supercapacitor with an ultrahigh energy density. Nano Lett. **10**, 4863–4868 (2010). https://doi.org/10.1021/nl102661q

7. Jain, A., Manippady, S.R., Tang, R., Nishihara, H., Sobczak, K., Matejka, V., Michalska, M.: Vanadium oxide nanorods as an electrode material for solid state supercapacitor. Sci. Rep. **12**, 1–12 (2022). https://doi.org/10.1038/s41598-022-25707-z
8. Inci Yesilyurt, E., Pionteck, J., Simon, F., Voit, B.: Fabrication of PANI/MWCNT supercapacitors based on a chitosan binder and aqueous electrolyte for enhanced energy storage. RSC Appl. Polym. **1**, 97–110 (2023). https://doi.org/10.1039/d3lp00061c
9. Kumar, A., Jena, H.M.: Preparation and characterization of high surface area activated carbon from Fox nut (Euryale ferox) shell by chemical activation with H3PO4. Results Phys. **6**, 651–658 (2016). https://doi.org/10.1016/j.rinp.2016.09.012
10. Yang, I., Jung, M., Kim, M.S., Choi, D., Jung, J.C.: Physical and chemical activation mechanisms of carbon materials based on the microdomain model. J. Mater. Chem. Mater. **9**, 9815–9825 (2021). https://doi.org/10.1039/d1ta00765c
11. Guo, Y., Yu, K., Wang, Z., - Carbon, H.X.: undefined Effects of activation conditions on preparation of porous carbon from rice husk, Ui.Adsabs.Harvard.Edu n.d. (2003). https://ui.adsabs.harvard.edu/abs/2003Carbo.41.1645G/abstract). (accessed November 10, 2024)
12. Lozano-Castello, D., Carbon, M.L.-R.-., Preparation of activated carbons from Spanish anthracite: I. Activation by KOH, Elsevier: undefined (n.d.). (2001). https://www.sciencedirect.com/science/article/pii/S0008622300001858 (accessed November 10, 2024)
13. Lillo-Ródenas, M., Carbon, D.L.-C.-.: undefined Preparation of activated carbons from Spanish anthracite: II. Activation by NaOH, Elsevier (n.d.). (2001). https://www.sciencedirect.com/science/article/pii/S000862230000186X (accessed November 10, 2024)
14. Chun, S., J.W.-M. and, Materials, M.: undefined Formation of micro/mesopores during chemical activation in tailor-made non-graphitic carbons, ElsevierSE Chun, JF WhitacreMicroporous and Mesoporous Materials, 2017•Elsevier (n.d.). (2017). https://www.sciencedirect.com/science/article/pii/S1387181117303657 (accessed November 10, 2024)
15. Chew, T.W., H'Ng, P.S., Luqman Chuah Abdullah, B.C.T.G., Chin, K.L., Lee, C.L., Mohd Nor Hafizuddin, B.M.S., TaungMai, L.: A review of Bio-based activated Carbon Properties produced from different activating chemicals during chemicals activation process on Biomass and its potential for Malaysia. Materials. **16** (2023). https://doi.org/10.3390/ma16237365
16. Ji, T., Han, K., Teng, Z., Li, J., Wang, M., Zhang, J., Cao, Y., Qi, J.: Synthesis of activated Carbon Derived from Garlic Peel and its Electrochemical properties. Int. J. Electrochem. Sci. **16**, 1–14 (2021). https://doi.org/10.20964/2021.01.61
17. Qian, W., Sun, F., Xu, Y., Qiu, L., Liu, C., Wang, S., Yan, F.: Human hair-derived carbon flakes for electrochemical supercapacitors. Energy Environ. Sci. **7**, 379–386 (2014). https://doi.org/10.1039/c3ee43111h
18. Liang, S.X., Duan, F.F., Lü, Q.F., Yang, H.: Hierarchical biocarbons with controlled micropores and mesopores derived from Kapok Fruit peels for high-performance Supercapacitor Electrodes. ACS Omega. **4**, 5991–5999 (2019). https://doi.org/10.1021/acsomega.9b00148
19. Tarimo, D.J., Oyedotun, K.O., Sylla, N.F., Mirghni, A.A., Ndiaye, N.M., Manyala, N.: Waste chicken bone-derived porous carbon materials as high performance electrode for supercapacitor applications. J. Energy Storage. **51**, 104378 (2022). https://doi.org/10.1016/j.est.2022.104378
20. Wu, L., Li, Y., Fu, Z., Su, B.L.: Hierarchically structured porous materials: Synthesis strategies and applications in energy storage. Natl. Sci. Rev. **7**, 1667–1701 (2020). https://doi.org/10.1093/nsr/nwaa183
21. Michael, M.S., Surya, K.: Feasibility study on conversion of biowaste of lemon peel into carbon electrode for supercapacitor using ZnCl2 as an activating agent. Mater. Renew. Sustain. Energy. 1–12 (2024). https://doi.org/10.1007/S40243-024-00273-8/TABLES/3
22. Zhang, K., Sun, J., Ma, L.E.C., Luo, S., Wu, Z., Li, W., Liu, S.: Effects of the Pore structure of Commercial activated Carbon on the Electrochemical performance of Supercapacitors. J. Energy Storage. **45**, 103457 (2022). https://doi.org/10.1016/j.est.2021.103457
23. Zhu, Z., Jiang, H., Guo, S., Cheng, Q., Hu, Y., Li, C.: Dual tuning of Biomass-Derived Hierarchical Carbon nanostructures for Supercapacitors: The role of Balanced Meso/Microporosity and Graphene. Sci. Rep. **5**, 1–9 (2015). https://doi.org/10.1038/srep15936
24. Xia, K., Gao, Q., Jiang, J., Hu, J.: Hierarchical porous carbons with controlled micropores and mesopores for supercapacitor electrode materials. Carbon N Y. **46**, 1718–1726 (2008). https://doi.org/10.1016/j.carbon.2008.07.018
25. Ahmed, M.J., Islam, M.A., Asif, M., Hameed, B.H.: Human hair-derived high surface area porous carbon material for the adsorption isotherm and kinetics of tetracycline antibiotics. Bioresour Technol. **243**, 778–784 (2017). https://doi.org/10.1016/j.biortech.2017.06.174
26. Lillo-Ródenas, M.A., Cazorla-Amorós, D., Linares-Solano, A.: Understanding chemical reactions between carbons and NaOH and KOH: An insight into the chemical activation mechanism. Carbon N Y. **41**, 267–275 (2003). https://doi.org/10.1016/S0008-6223(02)00279-8
27. Wang, J.: accessed November 10, S.K.-J. of materials chemistry, undefined 2012, KOH activation of carbon-based materials for energy storage, Pubs.Rsc.OrgJ Wang, S KaskelJournal of Materials Chemistry, 2012•pubs.Rsc.Org (n.d.) (2024). https://pubs.rsc.org/en/content/articlehtml/2010/m9/c2jm34066f)
28. Lozano-Castelló, D., Calo, J.M., Cazorla-Amorós, D., Linares-Solano, A.: Carbon activation with KOH as explored by temperature programmed techniques, and the effects of hydrogen. Carbon N Y. **45**, 2529–2536 (2007). https://doi.org/10.1016/J.CARBON.2007.08.021
29. Bu, Y., Liang, H., Shi, R., Liu, H., Zhang, Y., Sun, T., Lian, C., Shen, X., Li, H.: Assessing the Maximum Power and Consistency of Carbon Supercapacitors through a facile practical strategy. ACS Sustain. Chem. Eng. **8**, 12430–12436 (2020). https://pubs.acs.org/doi/10.1021/acssuschemeng.0c03039
30. Maphiri, V.M., Bakhoum, D.T., Sarr, S., Sylla, N.F., Rutavi, G., Manyala, N.: Low temperature thermally reduced graphene oxide directly on Ni-Foam using atmospheric pressure-chemical vapour deposition for high performance supercapacitor application. J. Energy Storage. **52**, 104967 (2022). https://doi.org/10.1016/j.est.2022.104967
31. Xing, Z., Qi, Y., Tian, Z., Xu, J., Yuan, Y., Bommier, C., Lu, J., Tong, W., Jiang, D.E., Ji, X.: Identify the removable substructure in Carbon Activation. Chem. Mater. **29**, 7288–7295 (2017). https://doi.org/10.1021/acs.chemmater.7b01937
32. TUINSTRA, F., KOENIG, J.L.: Raman Spectrum of Graphite. J. Chem. Phys. **53**, 1126–1130 (1970). https://doi.org/10.1063/1.1674108
33. Zhao, Y., Cho, C.W., Cui, L., Wei, W., Cai, J., Wu, G., Yun, Y.S.: Adsorptive removal of endocrine-disrupting compounds and a pharmaceutical using activated charcoal from aqueous solution: Kinetics, equilibrium, and mechanism studies. Environ. Sci. Pollut. Res. **26**, 33897–33905 (2019). https://doi.org/10.1007/S11356-018-2617-7
34. Muniandy, L., Adam, F., Mohamed, A., E.N.-M. and, Mesoporous, The synthesis and characterization of high purity mixed microporous/mesoporous activated carbon from rice husk using chemical activation with NaOH and, Muniandy, E.L., Adam, F., Mohamed, A.R.: undefined, EP NgMicroporous and Mesoporous

Materials, 2014•Elsevier (n.d.). (2014). https://www.sciencedirect.com/science/article/pii/S1387181114003382 (accessed November 10, 2024)
35. Abdulsalam, J., Mulopo, J., Oboirien, B., Bada, S., Falcon, R.: Experimental evaluation of activated carbon derived from South Africa discard coal for natural gas storage. Int. J. Coal Sci. Technol. **6**, 459–477 (2019). https://doi.org/10.1007/S40789-019-0262-5
36. Neimark, A., Lin, Y., Ravikovitch, P., - Carbon, M.T.: undefined Quenched solid density functional theory and pore size analysis of micro-mesoporous carbons, ElsevierAV Neimark, Y Lin, PI Ravikovitch, M ThommesCarbon, 2009•Elsevier (n.d.). (2009). https://www.sciencedirect.com/science/article/pii/S000862230900633 (accessed September 13, 2024)
37. Li, S., Tan, X., Li, H., Gao, Y., Wang, Q., Li, G., Guo, M.: Investigation on pore structure regulation of activated carbon derived from sargassum and its application in supercapacitor. Sci. Rep. 2022. **12**(12), 1 (2022). https://doi.org/10.1038/s41598-022-14214-w
38. Suárez, L., Barranco, V., Centeno, T.A.: Impact of carbon pores size on ionic liquid based-supercapacitor performance. J. Colloid Interface Sci. **588**, 705–712 (2021). https://doi.org/10.1016/j.jcis.2020.11.093
39. Qian, Y., Jiang, S., Li, Y., Yi, Z., Zhou, J., Tian, J., Lin, N., Qian, Y.: Understanding mesopore volume-enhanced extra-capacity: Optimizing mesoporous carbon for high-rate and long-life potassium-storage. Energy Storage Mater. **29**, 341–349 (2020). https://doi.org/10.1016/j.ensm.2020.04.026
40. Zhong, C., Deng, Y., Hu, W., Qiao, J., Zhang, L., Zhang, J.: A review of electrolyte materials and compositions for electrochemical supercapacitors. Chem. Soc. Rev. **44**, 7484–7539 (2015). https://doi.org/10.1039/c5cs00303b
41. Mirghni, A.A., Oyedotun, K.O., Mahmoud, B.A., Fasakin, O., Tarimo, D.J., Manyala, N.: A study of co-mn phosphate supported with graphene foam as promising electrode materials for future electrochemical capacitors. Int. J. Energy Res. **46**, 3080–3094 (2022). https://doi.org/10.1002/er.7365
42. Sudhan, N., Subramani, K., Karnan, M., Ilayaraja, N., Sathish, M.: Biomass-derived activated porous carbon from rice straw for a high-energy symmetric supercapacitor in aqueous and nonaqueous electrolytes. Energy Fuels. **31**, 977–985 (2017). https://doi.org/10.1021/acs.energyfuels.6b01829
43. Niu, L., Shen, C., Yan, L., Zhang, J., Lin, Y., Gong, Y., Li, C., Sun, C.Q., Xu, S.: Waste bones derived nitrogen–doped carbon with high micropore ratio towards supercapacitor applications. J. Colloid Interface Sci. **547**, 92–101 (2019). https://doi.org/10.1016/j.jcis.2019.03.097
44. Manasa, P., Lei, Z.J., Ran, F.: Biomass Waste Derived low cost activated Carbon from Carchorus Olitorius (jute Fiber) as sustainable and Novel Electrode Material. J. Energy Storage. **30**, 101494 (2020). https://doi.org/10.1016/j.est.2020.101494
45. Chen, D., Li, Z., Jiang, J., Wu, J., Shu, N., Zhang, X.: Influence of electrolyte ions on rechargeable supercapacitor for high value-added conversion of low-grade waste heat. J. Power Sources. **465**, 228263 (2020). https://doi.org/10.1016/j.jpowsour.2020.228263
46. Kitenge, V.N., Tarimo, D.J., Oyedotun, K.O., Rutavi, G., Manyala, N.: Facile and sustainable technique to produce low-cost high surface area mangosteen shell activated carbon for supercapacitors applications. J. Energy Storage. **56**, 105876 (2022). https://doi.org/10.1016/j.est.2022.105876
47. Fasakin, O., Dangbegnon, J.K., Momodu, D.Y., Madito, M.J., Oyedotun, K.O., Eleruja, M.A., Manyala, N.: Synthesis and characterization of porous carbon derived from activated banana peels with hierarchical porosity for improved electrochemical performance. Electrochim. Acta. **262**, 187–196 (2018). https://doi.org/10.1016/j.electacta.2018.01.028
48. Arunkumar, M., omega, A.P.-A.: undefined Importance of electrode preparation methodologies in supercapacitor applications, Ncbi.Nlm.Nih.Gov n.d. (2017). https://www.ncbi.nlm.nih.gov/pmc/articles/PMC6645427/). (accessed November 28, 2024)
49. Gao, P., Tsai, W., Daffos, B., Taberna, P., Energy, C.P.-N.: undefined Graphene-like carbide derived carbon for high-power supercapacitors, ElsevierPC Gao, WY Tsai, B Daffos, PL Taberna, CR Pérez, Y Gogotsi, P Simon, F FavierNano Energy, 2015•Elsevier (n.d.). (2015). https://www.sciencedirect.com/science/article/pii/S2211285514002869 (accessed November 28, 2024)
50. Taer, E., Apriwandi, A., Proceedings, R.T.-M.T.: undefined 3D meso-macroporous carbon derived spruce leaf biomass for excellent electrochemical symmetrical supercapacitor, Elsevier (n.d.). (2023). https://www.sciencedirect.com/science/article/pii/S2214785323004662 (accessed November 29, 2024)